The Astronomical Journal, 142:19 (9pp), 2011 July doi:10.1088/0004-6256/142/1/19

SPECKLE CAMERA OBSERVATIONS FOR THE NASA *KEPLER* MISSION FOLLOW-UP PROGRAM

Steve B. Howell[1,2], Mark E. Everett[1], William Sherry[3], Elliott Horch[4], and David R. Ciardi[5]
[1] National Optical Astronomy Observatory, Tucson, AZ 85719, USA
[2] NASA Ames Research Center, Moffett Field, CA 94035, USA
[3] National Solar Observatory, Tucson, AZ 85719, USA
[4] Department of Physics, Southern Connecticut State University, New Haven, CT 06515, USA
[5] NASA Exoplanet Science Institute, California Institute of Technology, Pasadena, CA 91125, USA
Received 2011 April 11; accepted 2011 April 29; published 2011 June 8

ABSTRACT

We present the first results from a speckle imaging survey of stars classified as candidate exoplanet host stars discovered by the *Kepler* mission. We use speckle imaging to search for faint companions or closely aligned background stars that could contribute flux to the *Kepler* light curves of their brighter neighbors. Background stars are expected to contribute significantly to the pool of false positive candidate transiting exoplanets discovered by the *Kepler* mission, especially in the case that the faint neighbors are eclipsing binary stars. Here, we describe our *Kepler* follow-up observing program, the speckle imaging camera used, our data reduction, and astrometric and photometric performance. *Kepler* stars range from $R = 8$ to 16 and our observations attempt to provide background non-detection limits 5–6 mag fainter and binary separations of ∼0.05–2.0 arcsec. We present data describing the relative brightness, separation, and position angles for secondary sources, as well as relative plate limits for non-detection of faint nearby stars around each of 156 target stars. Faint neighbors were found near 10 of the stars.

Key words: instrumentation: high angular resolution – planets and satellites: general – techniques: photometric

Online-only material: machine-readable and VO tables

1. MOTIVATION

Speckle observations have traditionally been used to observe relatively bright stars to search for close binaries and, through continued observation, trace the orbit of companions and characterize stellar binaries for applications in fundamental astrophysics. Typical speckle camera studies target stars in the range $V = 4$–10 and can detect and measure binary separations of ∼0.05–2.0 arcsec. At these separations, speckle observations can detect real companions as close as a few AU for stars within 200 pc of the Sun. Horch et al. (2008, 2010) provide examples of the use of speckle observations in a program to determine orbits and other astrophysical properties for a large set of *Hipparcos* double and suspected double stars.

Our interest in speckle observations as a part of the follow-up program for the exoplanet mission *Kepler* (Borucki et al. 2010) is to search for companion or spatially aligned background stars, not for orbit determination, but to help exclude (or validate) candidate transiting exoplanets. When transit-like events are found in the light curve of a star targeted by these missions, the star becomes a candidate exoplanet host if it passes a series of tests based on the satellite data and any stellar properties known a priori (Batalha et al. 2010). Even after the candidate passes these initial tests, there are potential phenomena other than a transiting exoplanet that could be producing a false transit-like signal. The most likely source for such a false positive is a background eclipsing binary star nearly spatially coincident with the target star (Brown 2003). By measuring the brightness and location of any faint stars near the candidate stars, we can help to determine whether contaminating flux from those nearby stars could be responsible for the transit-like signals.

False positive elimination of transiting exoplanet candidates imposes different requirements on speckle imaging than its more typical applications. While it is still important to detect companions and measure their magnitude difference and location, transit follow-up requires observations of fainter target stars (to $V \sim 16$), deeper and well-defined non-detection limits, detecting companions as nearby as possible, and slightly different data collection and reduction techniques due to our need to co-add multiple frames taken over a longer than usual time (15–30 minutes).

To meet these observational requirements, we have upgraded the Differential Speckle Survey Instrument (DSSI; Horch et al. 2009) used at the WIYN telescope on Kitt Peak. The new upgrades are described in Horch et al. (2010). The most important upgrade is the use of two new electron multiplier CCDs (EMCCDs, also known as low light level or L3 CCDs) to obtain observations in two filters simultaneously. Other upgrades include a "real-time" data reduction pipeline and a new suite of analysis tools.

Below, we describe some of the details of the new DSSI instrument specific to our work on the *Kepler* follow-up program. This is followed by a summary of the observational, data reduction, and analysis methods. Finally, we present results from our study of *Kepler* mission exoplanet transit candidates.

2. DUAL EMCCD SPECKLE CAMERA

Figure 1 shows the DSSI speckle instrument mounted on the WIYN telescope. The two Andor iXon 897 EMCCDs are seen attached at perpendicular ports. Each EMCCD is a 512 × 512 16 μm pixel frame transfer CCD. The iXon cameras have up to a 10 mHz pixel readout rate and are thermoelectrically cooled to as low as −100°C. Within the DSSI optics box, a changeable dichroic splits the beam and sends light to both cameras, allowing simultaneous observations through two filters, one placed in front of each EMCCD. Tokovinin & Cantarutti (2008) and Horch et al. (2010) provide discussions of the benefits of

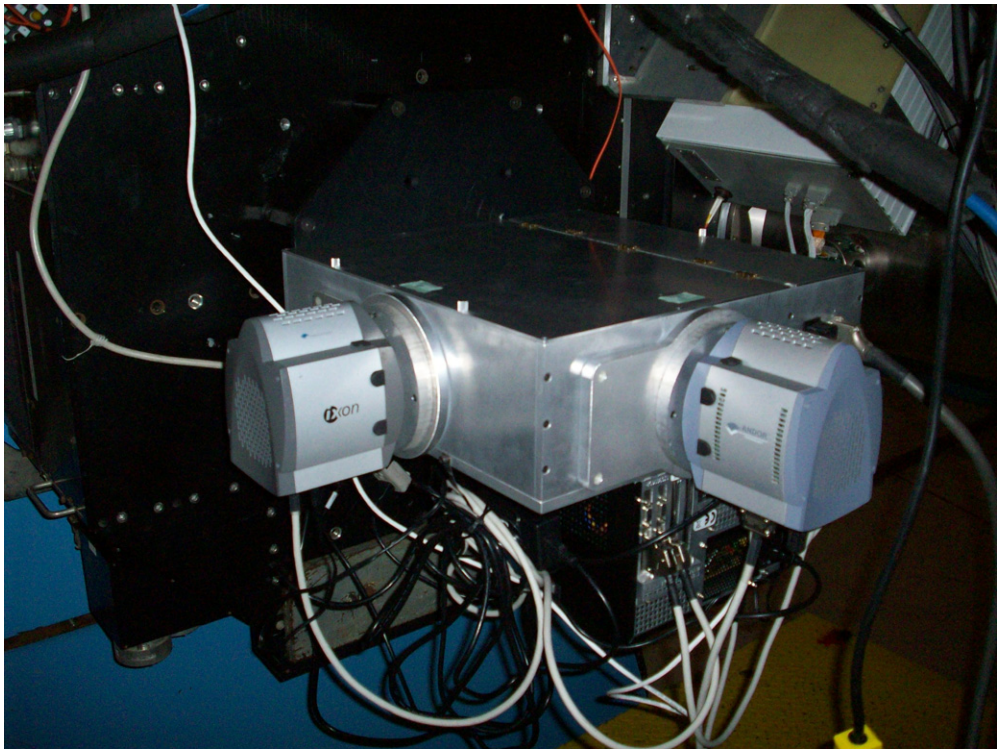

Figure 1. DSSI speckle camera with its two EMCCDs mounted on the WIYN telescope. The aluminum box contains the optics (field lens, beam splitter, and filters) and the two iXon EMCCD cameras are seen mounted at perpendicular ports. Attached below the aluminum box is the computer which runs the instrument and both cameras.

using EMCCDs for speckle observations including the on-CCD gain and insignificant read noise (even with fast readout).

The plate scale and on-sky orientation of the two speckle camera images are determined each night of operation or if some instrument property is changed (e.g., a filter change). Once or twice a run, a slit mask is placed at the tertiary mirror baffle support of the alt-az WIYN telescope. We obtain a speckle image of a bright star observed through the mask for which the power spectrum relates directly to the slit spacing and thus to the plate scale of our speckle images. Our plate scales are determined to be 0.021765 and 0.022816 arcsec pixel^{-1} ($\pm$0.1%) for the two cameras. Detector orientation is established for the speckle images using short exposures of bright stars interspersed with known telescope offsets. Details of the procedures discussed here are given in Horch et al. (2010).

3. OBSERVING STRATEGY

Our general speckle observing procedures have been described in Horch et al. (2010). Here we present additional procedures we have tested and applied to our *Kepler* target star observations. The major change from typical speckle observing procedures is the need to observe fainter target stars and provide deeper non-detection limits as required for the *Kepler* follow-up program. *Kepler* stars range from $R = 8$ to 16 and our observations attempt to provide background non-detection limits 5–6 mag fainter and binary separations of $\sim$0.05–2.0 arcsec.

At the short sample times of speckle observations, typically near 30 ms, photon starvation is the largest detriment to data quality. Typically, for bright stars, we obtain 1000 30–40 ms samples to co-add during data reduction. For our fainter targets, we needed to come up with a strategy which kept the signal-to-noise ratio (S/N) high, yet allowed for speckle imaging at $R = 13$–16 mag.

For a given telescope aperture and site location, the atmospheric coherence time for speckle patterns is known to scale approximately linearly with the Fried parameter; the S/N obtainable in a speckle observation has been studied in detail by, e.g., Welsh (1995). That work shows that the curve of S/N versus frame integration time is expected to have a maximum that is related to the atmospheric correlation time but that the exact value is affected by detector and telescope parameters. At WIYN, speckle imaging has been undertaken for over 10 years and typically $\sim$30–40 ms exposure times have been used for each frame. Using the known speckle standard single star HR 6332, we conducted a test of varying the speckle sample time and determining the relative S/N of the measurement. Figure 2 presents our results obtained on UT 2010 June 20, a night with $\sim$0.″9 FWHM native seeing at WIYN, a value poorer than usual for this telescope (the median is 0.″6 FWHM). The S/N values plotted are the average S/N within a thin annulus centered at half the diffraction limit in the power spectrum of the observation, a typical way to characterize S/N in speckle imaging. The two curves represent simultaneous measurements in 692 nm and 562 nm filters with 1σ errors shown. This brief test shows what had been common practice all along at WIYN, that is, sampling times of 30–40 ms provide the best match between the shortest sampling times with the best atmospheric coherence. Longer sampling times with more photons, but poorer atmospheric coherence reveal that the S/N (and thus spatial resolution) decreases approximately linearly with time. At 80 ms (see below) we would typically obtain an S/N which is only about 1/3 of that which we would get at 30 ms for the same total integration time and native seeing. S/N in speckle observations is proportional to the square root of the number of frames obtained ($\sim$total integration time) and scales as the Fried

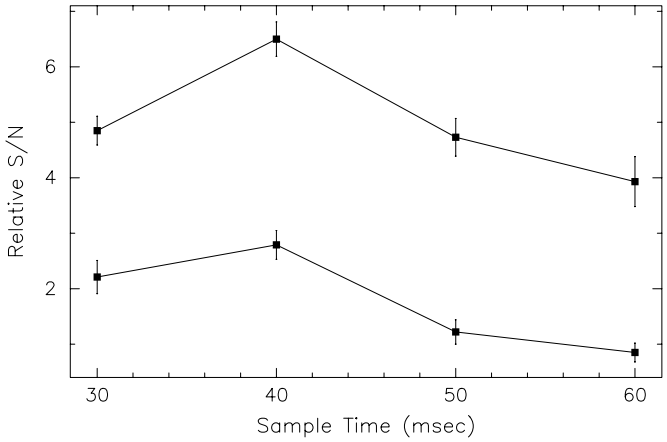

Figure 2. S/N vs. sampling time test using the bright single star HR 6332. The relative S/N is the average value from a thin annulus centered at half the diffraction limit in the power spectrum of the observation. The top curve is for the 692/40 nm filter, while the bottom curve is for the 562/40 nm filter. For the 3.5 m WIYN telescope, sample times of 40 ms provide slightly better S/N than 30 ms, while the S/N falls slowly for longer sample times due to loss of atmospheric coherence. The error bars are 1σ values.

parameter squared, so as $1/\text{seeing}^2$ (seeing here means the seeing FWHM). Thus, for a good night, 80 ms sampling collected for 3000–5000 images produces nearly the same S/N in the final reconstructed image as one 1000 frame 40 ms set would for a brighter star. The major drawback is reduced spatial resolution (to nearly 0.″1) when using longer sample times due to the loss of atmospheric coherence.

Our observing strategy for most targets has therefore become the following. On a clear night with good native seeing and usually at an airmass less than 1.6, we collect 1000 40 ms frames if the target is sufficiently bright ($R \leqslant 10$), two sets of 1000 frames each if $10 < R \leqslant 11.5$, three sets of 1000 frames each if $11.5 < R \leqslant 12$, and 5 sets of 1000 frames each if $12 < R \leqslant 13.5$. For fainter targets ($R > 13.5$) or on non-optimal nights, we use 80 ms samples and collect 3–5 sets of 1000 frames each. A plot of the time on the sky used to observe targets as a function of their *Kepler* magnitude is shown in Figure 3. The *Kepler* magnitude is an estimated magnitude for the *Kepler* bandpass as calculated in the *Kepler* Input Catalog (Brown et al. 2011).

We routinely read out a 128 × 128 pixel subregion of the EMCCDs, centering each readout region on the target star in order to capture its entire speckle pattern. This subregion yields a 2.″8 × 2.″8 field of view. The reasons are twofold: (1) reading the full 512 × 512 frame takes more time, so you get fewer frames a second, and cannot keep up with the atmosphere and (2) a single 1000 full frame observation would then be 1 GB in each filter, a bit impractical for survey work. We have used combinations of three different filters for our observations. Between 2010 June 18 and September 20, we used filters with central wavelengths and widths of $\lambda_C = 562$ nm, $\Delta\lambda = 40$ nm and $\lambda_C = 692$ nm, $\Delta\lambda = 40$ nm. Between 2010 September 21 and October 25, we replaced the 562 nm filter with one having $\lambda_C = 880$ nm, $\Delta\lambda = 50$ nm.

4. DATA REDUCTION

Candidate transiting planet host stars are vetted through a number of ground-based observing programs in addition to speckle imaging. Ground-based observations of the *Kepler* field of view are practical only during a limited observing season,

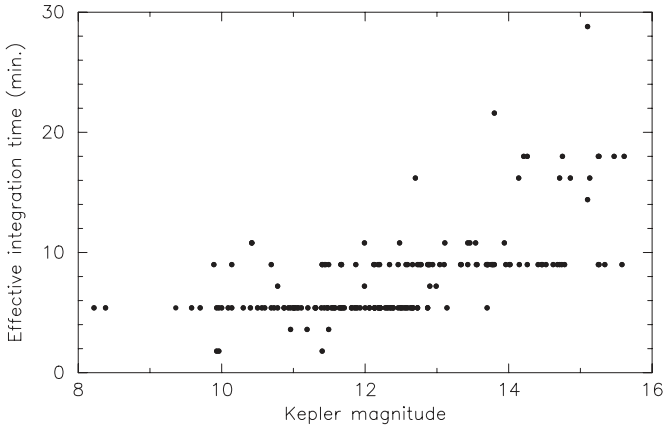

Figure 3. Time spent on the sky (including our duty cycle) used to observe *Kepler* target stars of different magnitudes.

so high priority transit candidates are observed by different *Kepler* follow-up observing programs in a short span of time. This makes it urgent that speckle observations of a target are processed and analyzed promptly to detect any nearby companions which could affect the observing priorities of the other programs. To accomplish this, we have written a software pipeline to process a night's observations up to the point where the results are ready for our final manual inspection. This final interactive step allows us to refit fringe models if necessary, and provide a classification (single or not) for each source. We start this pipeline program at the end of each night's observations. Normally, the data are fully processed and ready for inspection by the following afternoon.

Our pipeline sorts the data into sets which were taken in the same region of the sky at roughly similar times. It then matches each science target with the point source observation which is the closest match in declination and hour angle.

The pipeline first calculates the autocorrelation for each frame of the image set. This searches the images for groups of speckles with the same separation and orientation. Binaries or other pairs of stars have speckle patterns that contain pairs of speckles (one speckle per star). Triple systems have groups of three speckles. The autocorrelation for all the frames in an image set are added together. The pipeline identifies objects which have multiple observations and sums the autocorrelation files to improve signal to noise.

Next, the pipeline calculates the power spectrum for each observation. The power spectrum is the Fourier transform of the summed autocorrelation for each set of images. The power spectrum of each science target is divided by the power spectrum of the corresponding point source to produce an image of the fringe pattern of the science target. The pipeline then uses the summed Fourier pattern of the data to make a reconstructed image of the source determined by bispectral analysis. The bispectrum provides the phase information of the object's Fourier transform, which in the case of a binary star, resolves the quadrant ambiguity that is present in the autocorrelation analysis.

We follow the above steps by running a procedure to estimate the location of the secondary in the reconstructed image, under the assumption that there are two stars in the field. The code locates a secondary peak in the reconstructed image, and its rough position is used to fit a model to the fringe pattern using a weighted least-squares method (Horch et al. 1996). As a result, the code always searches for a companion star, but

various metrics within the code as well as manual inspection of the reconstructed images allow us to identify true companions compared with those in which the algorithm has erroneously identified a noise spike or cosmic ray as the "secondary."

The final portion of our pipeline displays fringe patterns, the best-fit fringe model, and the reconstructed images of the target star. This portion of the program allows us to examine, for both filters, the reconstructed image and the noise of the reconstructed image, compare the fringe data to the fringe model, and interactively refit the fringe data if the match between the fringe data and model is poor. A genuine companion star will normally be observed in the same location in the reconstructed images from both filters. An exception would be when the secondary star is very faint in one of the filters, i.e., very red or very blue. The interactive pipeline permits the user to classify stars as doubles, triples, or unresolved single stars. Additionally, targets that are unresolved (at or below the diffraction limit) may produce a pattern with a single detectable fringe, indicating a possible very close pair. If a similar pattern is seen in multiple exposures and filters, as object will be classified as a "suspected double."

For true doubles, the pipeline calculates their separation (ρ), the position angle of the secondary (fainter source) relative to the primary (θ), their magnitude difference (Δm), and the native seeing. The values for ρ and θ are determined directly from the spacing and orientation of the model fringe pattern. The amplitude of the fringes in the best-fit model is used to determine Δm for the system.

In the case of a few doubles, the position angle (or quadrant) of the secondary is ambiguous by exactly 180°. This occurs when a pair of sources of comparable brightness representing the secondary appear on either side of the primary in our reconstructed images. In such cases, the pipeline user makes a best determination for the position angle based on all sets of images taken of the target. The ambiguous sources are noted in Table 2.

The quality of the observations and the properties of the stars limit the reliability of the measurements. When there are too few photons per 40 ms frame, either the autocorrelation routines fail, or are only sensitive to widely separated pairs.

The pipeline also calculates the quantity q' for doubles, which is defined as the product of the native seeing times ρ in arcsec^2 (Horch et al. 2001). We use the q' value as a check on the quality of the differential photometry. For doubles having a large value of q', Δm may be overestimated. As discussed by Horch et al. (2001), this arises due to two effects. There may be loss of flux from the secondary because its speckles wander out of the $2\farcs8 \times 2\farcs8$ field of view when the native seeing is poor and it lies close to the edge. Since the field of view is normally centered on the primary target star, its total flux will typically be conserved. Also, the components of widely separated doubles (which tend to have larger q' values) may not lie in the same isoplanatic patch so that their autocorrelation is weaker (especially for a faint companion) and the resulting fringe pattern will have lower amplitude corresponding to a larger Δm. For these data, we have adopted a value of $q' = 0.6$ as the rough threshold above which values of Δm are systematically high (see Horch et al. 2011).

4.1. Estimating Limiting Magnitudes in Speckle Images

In order to constrain the possibility that a background eclipsing binary star has produced a false positive transit-like signal in the *Kepler* light curves, it is important that we estimate the relative detection limit, or $\Delta m_{\max}$, that a star in the field could have while remaining detectable. Horch et al. (2011) have discussed the methods used to determine $\Delta m_{\max}$ in detail. Briefly, the method we use is as follows. We consider the distribution of all local minima and maxima in the background of the reconstructed images. We compute the standard deviation, σ, of these extrema from the mean background within a series of 5 0.″2 wide concentric annuli around the target star and placed at radii of 0.1–0.3, 0.3–0.5, 0.5–0.7, 0.7–0.9, and 0.9–1.1 arcsec from the target star. We define a conservative detection limit as being 5σ brighter than the mean background within each annulus. Figure 4 shows a typical result, a plot of the local extrema as a function of distance from the primary and the 5σ detection limit as a solid line fit through those values calculated for each annulus. The limiting magnitude depends upon the separation from the primary, but we have adopted the 5σ value at a separation of 0.″2 as the value we quote for $\Delta m_{\max}$. For separations less than 0.″2, $\Delta m_{\max}$ is somewhat smaller, while $\Delta m_{\max}$ is a bit larger for separations greater than 0.″2.

5. RESULTS

Our data reduction pipeline provides model fits and user's classifications for each target star. Data for 146 *Kepler* stars lacking definite secondary detections are presented in Table 1. Data for the 10 stars with detected secondaries are presented in Table 2. Note that KOI 13 corresponds to the known binary WDS 19079+4652 = A 704 and KOI 287 corresponds to the known binary COU 2691. Our results, obtained prior to knowledge of these two stars being doubles, generally agree with the previous measurements (however, see the note in Table 2 for KOI 287). None of the fields we have presented here show evidence for three or more stars. In each table, the stars are identified by a KOI (*Kepler* Object of Interest) number and *Kepler* ID number. The KOI numbers are used by the mission to refer to stars once they have been deemed transiting exoplanet candidates and are to undergo follow-up observations. The *Kepler* ID numbers are drawn from the *Kepler* Input Catalog, the mission's listing of all bright stars found within the *Kepler* field (Brown et al. 2011), although not necessarily selected for observation. Most of these stars are discussed in Borucki et al. (2011) while coordinates, photometric information, and light curves for all of the stars in Tables 1 and 2 can be found in the *Kepler* data archive at MAST[6] and the NASA Exoplanet database.[7] Table 1 also lists the *Kepler* magnitude, date of observation, integration time of each speckle image (of which 1000 such images were taken per co-added observation), the number of co-added observations, the central wavelength of the filter, our classification of the source, $\Delta m_{\max}$, and the native seeing.

For each star, we associate a value of the native seeing taken from measurements of a point source standard near our targets which we observe shortly before or afterward. For the 2010 observing season, we found mean FWHM of 0.″89 at 562 nm, 0.″83 at 692 nm, and 880 nm with standard deviations of 0.″26. Our data quality, particularly the very important detection limit for secondary stars, is highly dependent on native seeing.

Some of the stars presented in Table 1 show slightly elongated point-spread functions (PSFs) in their reconstructed images and a single strong fringe. These characteristics are typical of expectations for binaries with separations near our resolution limit of ~0.″05, but could also be the result of a mismatch between the PSFs of our target stars and reference stars (more specifically the main contribution is small differences in dispersion due to

[6] http://archive.stsci.edu/kepler/kepler_fov/search.php
[7] http://nexsci.caltech.edu/archives/nsted/

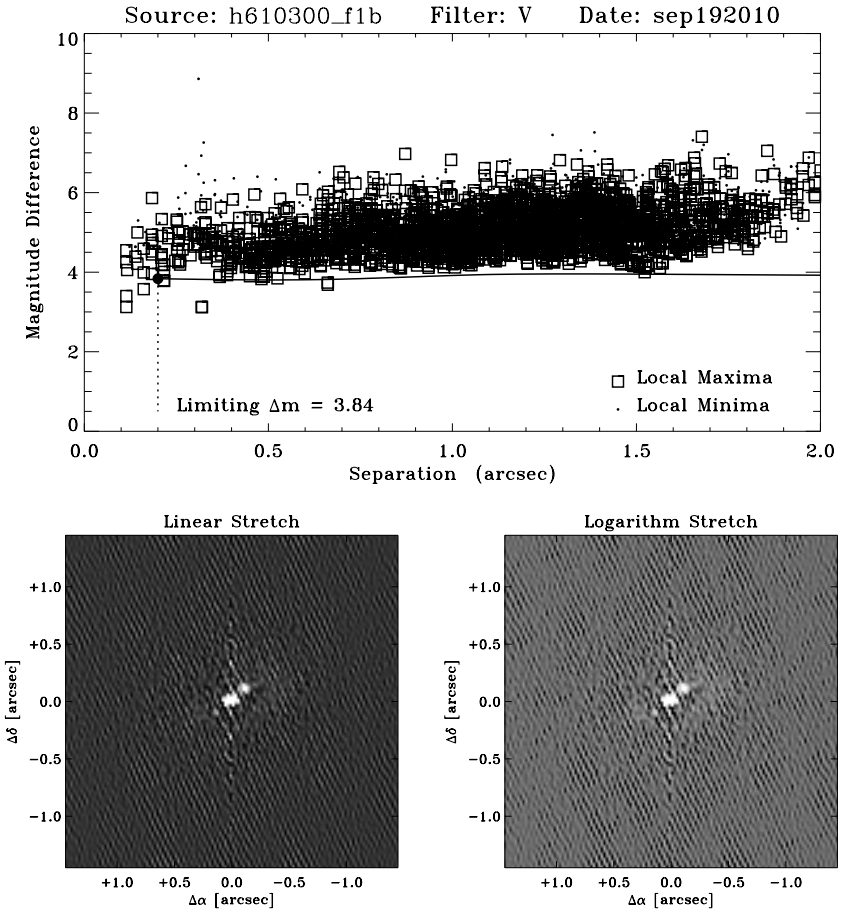

Figure 4. Results plot produced by our data reduction pipeline for KOI 300 in the 562 nm filter. The points in the top panel show the magnitude difference between the primary star and each of the local extrema measured in the background sky of our reconstructed Speckle image. The solid line shows the limiting magnitude relative to the primary star as defined by a flux that is five standard deviations brighter than the mean in the background as measured in concentric annuli centered on the primary. The dashed line shows the limiting magnitude value we define for this image, which is its value at a separation of 0.2 arcsec. A secondary star is identified by the pair of bright points with a separation of 0.″158, while other occasional bright artifacts in the image (e.g., cosmic rays) are rejected by software metrics and manual inspection. The bottom two panels show the reconstructed image with both a linear and logarithmic flux scale. North is at the top and east to the left and the companion is seen at a P.A. of 318 deg.

different sky positions between the point source and target and/or a large color difference between the target and point source). These suspected double stars are indicated with an "SD" as their classification. Future observations of these targets may confirm their nature.

Table 2 gives similar data as in Table 1, but additionally provides values derived from the fringe model fits to double stars. There are a number of stars that we have observed on multiple nights. These results, along with a comparison between results acquired on the two separate DSSI channels and previous experience using this instrument, permit an analysis of our astrometric and photometric precision and accuracy.

5.1. Astrometric Performance

A detailed analysis of the astrometric precision and accuracy for a large sample of binaries is given in Horch et al. (2011). Much of the data for those binaries were obtained on the same 2010 June nights as our *Kepler* target data and are representative of the performance we see in the data presented here. Horch et al. (2011) found good agreement in the position angle and separation measured for binaries in the 562 nm and 692 nm filters. The speckle data in the two filters represent independent astrometric measurements. For $\theta(562\,\mathrm{nm}) - \theta(692\,\mathrm{nm})$ they found a mean difference of $0.^\circ03 \pm 0.^\circ04$ with a standard deviation of $0.^\circ75 \pm 0.^\circ03$; scatter was less at larger separations, as would be expected given the dependence on linear measurement errors. For $\rho(562\,\mathrm{nm}) - \rho(692\,\mathrm{nm})$, the performance was equally as good with a mean of -0.01 ± 0.11 mas and standard deviation of 2.13 ± 0.08 mas. Horch et al. (2011) also examine the accuracy of their astrometry by comparing their results to that of other observers for a sample of binaries with well-determined orbits. For those binaries, no systematic differences in position angle or separation could be found.

For the *Kepler* follow-up data presented here, we make a similar comparison for double stars observed simultaneously in our two filters. We plot the differences in position angle and separation versus mean separation in Figure 5. We find a mean for $\Delta\rho$ of 0.56 ± 1.04 mas and mean $\Delta\theta$ of $-0.^\circ14 \pm 0.^\circ20$.

We can also compare results for doubles observed on multiple nights. The stars KOI 13, KOI 68, and KOI 98 were observed on two, three, and six different nights, respectively. Table 3 provides a summary of our mean measurements and 1σ uncertainties for the binary separations. Similarly, Table 4 presents a summary of our results for multiple measurements of position angle in these same three stars. These ranges are not inconsistent with the plots from Horch et al. (2011). In any case, the relative astrometry achieved with our methods provides the *Kepler* mission with sufficient accuracy to model the effects that neighboring stars have on *Kepler* light curves (e.g., Torres et al. 2011).

Table 1
Kepler Speckle Targets Lacking Detectable Secondaries

KOI	*Kepler* ID	*Kepler* Mag.	Date (UT)	Int. Time (ms)	Co-adds	λ_c (nm)	Classification[a]	Δm_{max}	Seeing ($''$)
4	3861595	11.43	2010 Sep 17	40	3	692	S	4.08	1.04
4	3861595	11.43	2010 Sep 17	40	3	562	S	4.38	1.30
4	3861595	11.43	2010 Sep 18	40	5	692	S	4.21	0.60
4	3861595	11.43	2010 Sep 18	40	5	562	S	4.84	0.71
5	8554498	11.67	2010 Sep 17	40	5	692	SD	3.98	1.04
5	8554498	11.67	2010 Sep 17	40	5	562	SD	4.49	1.30
5	8554498	11.67	2010 Sep 18	40	5	692	SD	4.53	0.58
5	8554498	11.67	2010 Sep 18	40	5	562	SD	4.27	0.63
5	8554498	11.67	2010 Sep 21	40	3	692	SD	4.22	0.93
5	8554498	11.67	2010 Sep 21	40	3	880	SD	3.54	0.89

Notes.
[a] S indicates single stars; SD indicates suspected doubles.
[b] KOIs 77, 78, and 79 are now known to be false positives.

(This table is available in its entirety in machine-readable and Virtual Observatory (VO) forms in the online journal. A portion is shown here for guidance regarding its form and content.)

Table 2
Kepler Speckle Targets with Detected Secondaries

KOI	*Kepler* ID	*Kepler* Mag.	Date (UT)	Int. Time (ms)	Co-adds	λ_c (nm)	ρ ($''$)	θ ($^\circ$)	Δm	Δm_{max}	Seeing ($''$)
13	9941662	9.96	2010 Jun 19	40	1	692	1.164	279.75	0.80	4.63	0.92
13	9941662	9.96	2010 Jun 19	40	1	562	1.165	279.56	0.83	3.46	0.88
13	9941662	9.96	2010 Jun 22	40	3	692	1.162	279.77	0.89	4.86	0.51
13	9941662	9.96	2010 Jun 22	40	3	562	1.162	279.64	1.22	4.89	0.58
42[a]	8866102	9.36	2010 Jun 20	40	3	692	...	...	...	4.96	1.09
42	8866102	9.36	2010 Jun 20	40	3	562	1.672	35.41	4.24	4.29	1.26
68	8669092	12.73	2010 Jun 21	40	3	692	0.748	256.45	2.98	3.70	0.91
68	8669092	12.73	2010 Jun 21	40	3	562	0.758	256.93	3.55	...	1.03
68	8669092	12.73	2010 Sep 17	40	3	692	0.735	256.73	2.82	3.39	0.77
68	8669092	12.73	2010 Sep 17	40	3	562	0.740	256.42	2.87	4.14	0.85
68	8669092	12.73	2010 Sep 18	40	5	692	0.738	256.79	2.83	3.23	0.59
68	8669092	12.73	2010 Sep 18	40	5	562	0.736	256.52	3.08	4.08	0.68
98	10264660	12.12	2010 Jun 19	40	5	692	0.290	143.66	0.94	3.69	0.92
98	10264660	12.12	2010 Jun 19	40	5	562	0.289	143.78	0.56	2.11	0.88
98	10264660	12.13	2010 Sep 19	40	3	692	0.289	143.71	0.48	2.82	0.62
98	10264660	12.13	2010 Sep 19	40	3	562	0.290	143.64	0.47	4.42	0.66
98	10264660	12.13	2010 Sep 20	40	5	692	0.289	143.67	1.12	2.97	1.18
98	10264660	12.13	2010 Sep 20	40	5	562	0.280	144.98	1.16	3.15	1.38
98	10264660	12.13	2010 Oct 23	40	3	692	0.290	143.96	0.53	3.64	0.67
98	10264660	12.13	2010 Oct 23	40	3	880	0.292	143.62	0.49	3.46	0.59
98	10264660	12.13	2010 Oct 24	40	3	692	0.289	143.74	0.61	3.95	0.90
98	10264660	12.13	2010 Oct 24	40	3	880	0.287	143.87	0.43	3.58	0.82
98	10264660	12.13	2010 Oct 25	40	3	692	0.289	143.29	1.04	3.53	0.58
98	10264660	12.13	2010 Oct 25	40	3	880	0.288	144.26	0.26	3.23	0.53
113	2306756	12.39	2010 Sep 19	40	3	692	0.176	166.67	1.63	3.58	0.67
113	2306756	12.39	2010 Sep 19	40	3	562	0.182	164.51	1.91	4.16	0.69
227[b]	6185476	14.26	2010 Jun 24	80	5	562	0.303	248.60	1.03	3.76	0.66
258	11231334	9.89	2010 Sep 19	40	5	692	1.013	72.99	3.64	4.57	1.11
258	11231334	9.89	2010 Sep 19	40	5	562	1.015	72.68	3.52	3.93	1.20
284	6021275	11.81	2010 Jun 24	40	3	692	0.871	97.14	0.94	4.37	0.93
284	6021275	11.81	2010 Jun 24	40	3	562	0.870	96.99	0.81	3.99	0.97
287[c]	8703887	11.05	2010 Sep 20	40	3	692	1.072	30.56	1.64	3.58	1.59
287[c]	8703887	11.05	2010 Sep 20	40	3	562	1.071	30.49	1.54	3.57	1.55
300	3438975	12.30	2010 Sep 19	40	3	692	0.164	318.23	1.84	3.95	0.59
300	3438975	12.30	2010 Sep 19	40	3	562	0.163	317.02	1.98	3.84	0.60

Notes.
[a] Secondary lies outside the slightly different field of view in this camera.
[b] Quadrant is ambiguous in our observations.
[c] Quadrant is ambiguous in our observations. *Tycho* measurements list the P.A. as 208 deg with a separation consistent with our value.

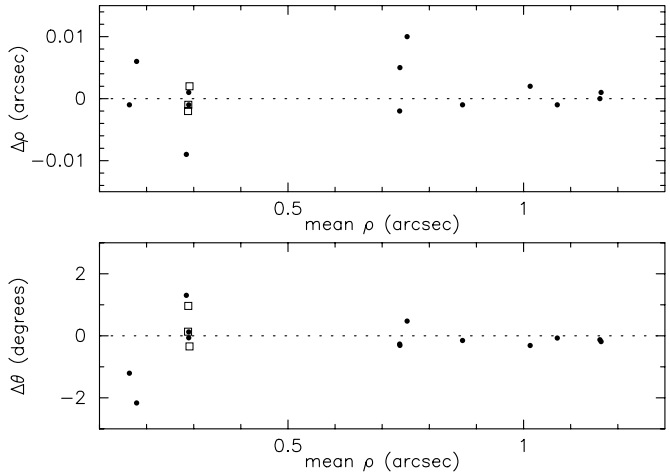

Figure 5. Differences in astrometric quantities for double stars measured simultaneously in two different filters. The top panel shows the difference in separation, $\Delta\rho$, vs. the mean separation. The values for $\Delta\rho$ are either $\rho(562\,\mathrm{nm}) - \rho(692\,\mathrm{nm})$ or $\rho(880\,\mathrm{nm}) - \rho(692\,\mathrm{nm})$ depending on the filters used for each observation. The bottom panel shows the difference in position angle, $\Delta\theta$, measured for the same stars vs. their mean separation. Similarly, the values for $\Delta\theta$ are either $\theta(562\,\mathrm{nm}) - \theta(692\,\mathrm{nm})$ or $\theta(880\,\mathrm{nm}) - \theta(692\,\mathrm{nm})$ depending on the filters used. In both panels, the open squares represent data comparing the 880 nm and 692 nm filters and filled circles represent data comparing the 562 nm and 692 nm filters.

Table 3
Astrometric Performance—Separation

KOI	λ	n	$\overline{\rho}$	σ^{a}
13	562	2	1.″163	0.″002
13	692	2	1.″164	0.″003
68	562	3	0.″740	0.″007
68	692	3	0.″745	0.″012
98	562	6	0.″289	0.″001
98	692	6	0.″286	0.″006
98	880	6	0.″289	0.″003

Note. [a] In cases of only two measurements, we give the difference between the measurements.

Table 4
Astrometric Performance—Position Angle

KOI	λ	n	$\overline{\theta}$	σ^{a}
13	562	2	279.°76	0.°02
13	692	2	279.°60	0.°08
68	562	3	256.°66	0.°18
68	692	3	256.°62	0.°27
98	562	6	143.°67	0.°22
98	692	6	144.°13	0.°74
98	880	6	143.°92	0.°32

Note. [a] In cases of only two measurements, we give the difference between the measurements.

5.2. Photometric Performance

The DSSI data provide a means to measure the relative fluxes for binary or double stars. The difference in the magnitude for each pair of stars, Δm, is an important part of our study because it affects the amount of contaminating flux that a secondary star will contribute to the *Kepler* light curves. Horch et al. (2011) examined their observations of known *Hipparcos* binaries in the 562 nm filter and compared their values for Δm to those taken from the *Hipparcos* Catalog. Because of the different

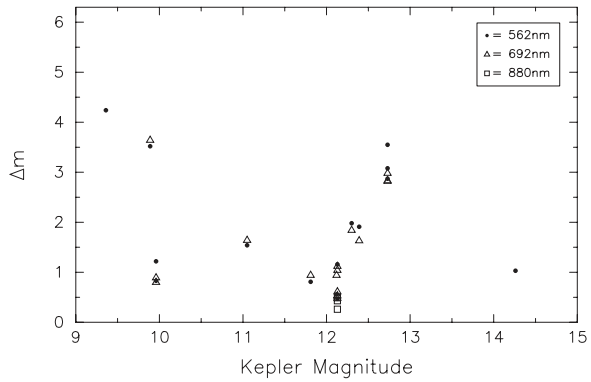

Figure 6. Magnitude differences between components in our double stars plotted vs. the *Kepler* magnitude. The different symbols represent observations taken through our 562 nm, 692 nm, and 880 nm filters.

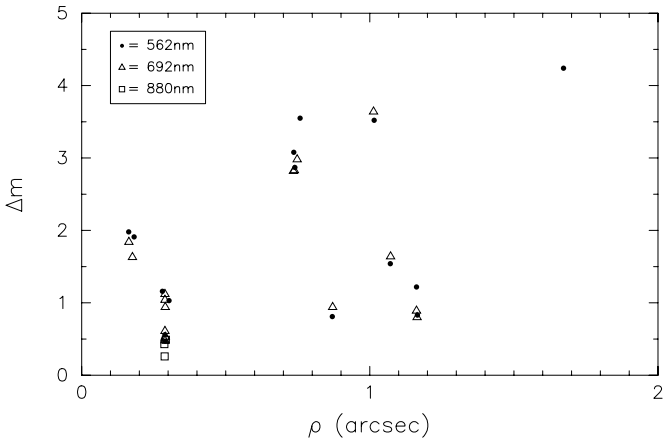

Figure 7. Magnitude differences in our double stars plotted vs. their separation. The different symbols represent observations taken through our 562 nm, 692 nm, and 880 nm filters.

bandpasses and in order to avoid instances where the quadrant of the secondary star could be ambiguous, they compared stars with the color $B - V < 0.6$, low uncertainties in their *Hipparcos* magnitude differences, and magnitude differences in the range $1.0 < \Delta m < 4.0$. Given the average uncertainty for the *Hipparcos* photometry, they derived a single measurement precision for $\Delta m(562\,\mathrm{nm})$ of 0.070 mag. Additionally, they examined how the agreement fared with increasingly large values of q'. Their results show that Δm values measured from the DSSI data agree well with those expected based on *Hipparcos* results until q' grows as high as 0.6 arcsec[2].

In Figure 6, we plot Δm versus the *Kepler* magnitude associated with each double source. In Figure 7, we plot Δm versus ρ for the same sources. In both of these figures, multiple pairs of points are clustered on the abscissa since three stars were observed on multiple nights. Table 5 examines our internal photometric precision based on these three doubles (KOI 13, KOI 68, and KOI 98) which were observed on two, three, and six nights, respectively.

5.3. Detection Limits

As equally important as measuring Δm for detectable secondary stars is measuring the detection limit of each speckle image, Δm_{max}, representing the maximum detectable difference in magnitudes fainter than the primary star for which we would detect secondaries. As described in Section 4.1, the detection limit is a function of separation from the primary, but we quote the detection limit at a separation of $\rho = 0.''2$ in Tables 1 and 2.

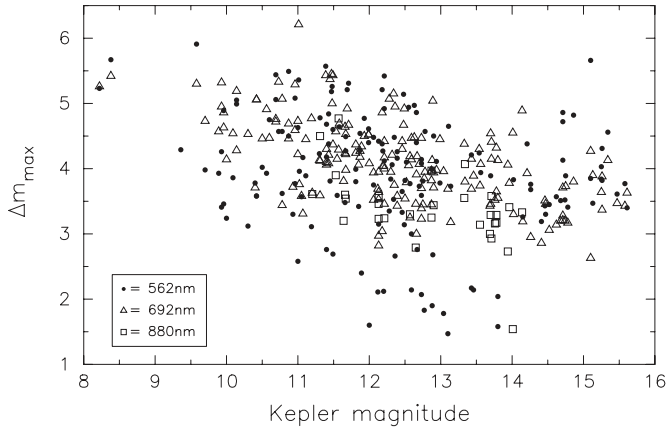

Figure 8. Plot of the detection limit relative to the primary star, $\Delta m_{\max}$, vs. *Kepler* magnitude for all targets. Points represent the detection limits measured at a separation distance of 0.″2 from the primary and different symbols denote observations in our 562 nm, 692 nm, and 880 nm filters. The lower 562 nm sequence is from a night of poor native seeing.

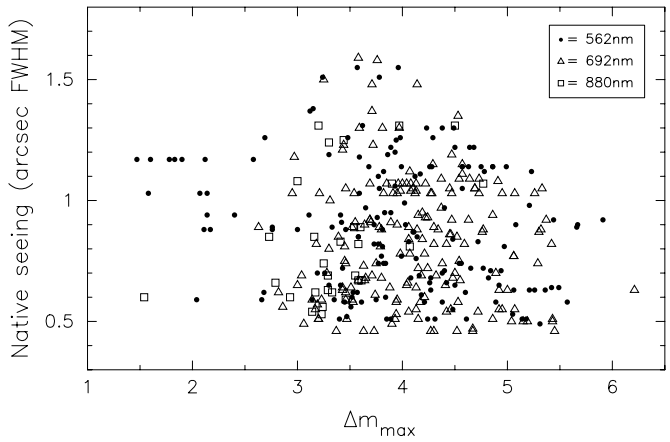

Figure 9. Plot of the native seeing determined for each observation vs. detection limit relative to the primary star, $\Delta m_{\max}$. Different symbols are used to indicate observations in our 562 nm, 692 nm, and 880 nm filters.

Table 5
Photometric Performance

KOI	λ	n	$\overline{\Delta m}$	σ [a]
13	562	2	0.85	0.09
13	692	2	1.03	0.39
68	562	3	2.88	0.09
68	692	3	3.17	0.35
98	562	6	0.79	0.28
98	692	6	0.73	0.38
98	880	6	0.39	0.12

Note. [a] In cases of only two measurements, we give the difference between the measurements.

The values for $\Delta m_{\max}$ found for each of our pointings are shown in Figure 8. The detection limit's dependence on native seeing can be seen in Figures 9 and 10. There is a lot of scatter, which in part may be attributable to differences in the exposure time used on different targets. In any case, better seeing generally led to deeper magnitude limits. Figure 10 shows that the deepest exposures, with plate limits fainter than 18th magnitude in the different filters, were achieved with seeing FWHM $\lesssim 1.''0$. Our plate limit dependence on integration time (time on the sky which includes both exposure and overhead time) is shown in Figure 11.

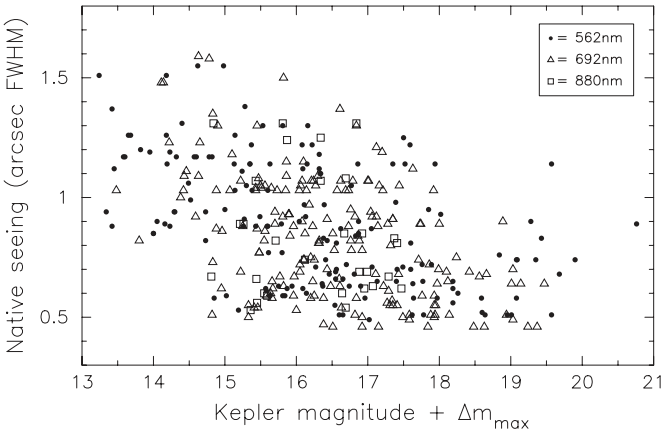

Figure 10. Plot of the native seeing determined for each observation vs. the sum of the *Kepler* magnitude and $\Delta m_{\max}$ for each observation. The abscissa values represent the plate limit. Different symbols are used to indicate observations in our 562 nm, 692 nm, and 880 nm filters.

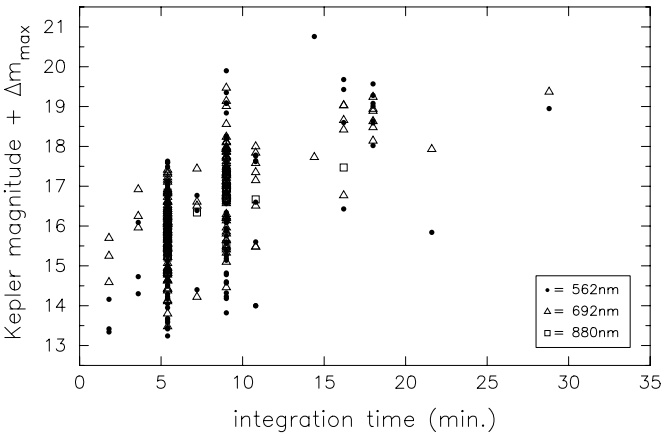

Figure 11. Plot of the sum of the *Kepler* magnitude and $\Delta m_{\max}$ (i.e., plate limit) vs. the time spent on the sky for each observation. The ordinate values represent the plate limit. Different symbols are used to indicate observations in our 562 nm, 692 nm, and 880 nm filters.

6. DOUBLE STAR CHARACTERISTICS

We examine the separation of our double sources in the hopes that we may learn whether they include many physical binaries or represent primarily a population of background stars. However, our sample only includes 10 doubles and is drawn from a slightly bias set of KOIs. That is, the KOIs observed were already searched in the *Kepler* data itself to determine if they produced detectable centroid shifts (i.e., $\gtrsim 2''$) coinciding with transit events in their light curves. If they did, they were removed from the KOI list.

If our sample of secondaries represents background stars, we would expect that they are randomly distributed throughout our field of view with only the detection limit's dependence on separation affecting the distribution. Our detection ability would make detecting faint secondaries at $\rho < 0.''2$ difficult and preclude detections at separations closer than our diffraction limit of $\sim 0.''05$. In Figure 12, we have plotted the fraction of secondary stars closer than a given separation from their primaries. Also plotted is the quadratic curve representing the distribution expected if their separations were random. The K-S statistic comparing the two distributions shows that our sample of doubles is consistent with a randomly distributed population of background stars. The closest separations in the

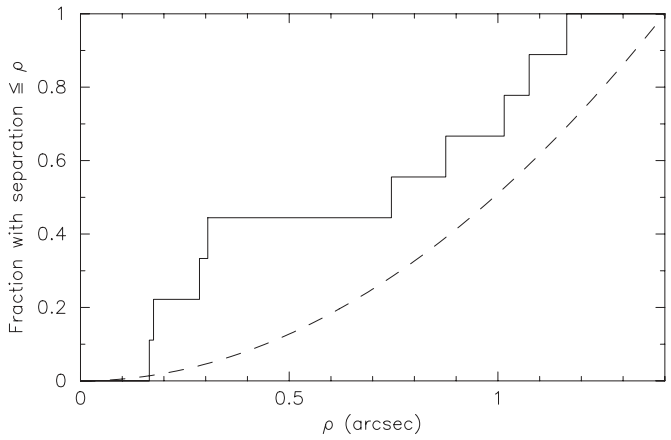

Figure 12. Plot of the fraction of all nine secondaries that lie closer than the separation, ρ, from their primary star as a function of separation (solid line). The choice of 1.″4 for the maximum ρ excludes one secondary star, but is the radius inside which our sample is complete given the 2.″8 × 2.″8 square field. The dashed line shows the distribution we would expect if secondaries were randomly distributed throughout the field and our detection limit were independent of ρ. See the text.

sample are for KOI 300 and 113, both with $\rho \simeq 0.''17$, or approximately the separation inside of which our detection limit drops significantly. While statistically consistent with a random distribution, we note that the dashed curve is below the data throughout the plot. This suggests that there may be two components to the separation distribution: a larger group of objects that is randomly distributed and a smaller group that is more clustered than random, i.e., physical pairs. Our sample of stars with companions is simply too small at present. A larger sample of doubles, which we expect to obtain from future observations, should help in our understanding of the population of secondary sources near *Kepler* targets.

7. CONCLUSIONS

We have presented the first results from our speckle imaging survey for sources near 156 *Kepler* objects of interest (KOIs; i.e., candidate transiting exoplanet host stars) discovered by the NASA *Kepler* mission. Faint sources near KOIs are known to be a significant source of false positive candidates since the flux from (typically fainter) eclipsing binaries may be blended with stars targeted by *Kepler*. In such cases, the blended stars may appear to exhibit transit-like signatures from planet-sized objects.

We have described our observing procedures, a new data reduction pipeline, and the dual-channel DSSI. DSSI provides a 2.″8 × 2.″8 field of view with resolution down to the optical diffraction limit at WIYN (∼0.″05), and by co-adding many exposures taken in a span as long as 30 minutes, we achieved a depth of detection that was typically 4 mag, but up to 6 mag fainter than the primary target star, dependent on seeing conditions and total exposure time. We found a total of 10 stars in our sample that have neighbors up to ∼4 mag fainter. We report on the secondary star locations and relative brightnesses that can be used in modeling the *Kepler* light curves as part of the candidate verification process. For each target, we also give a plate limit relative to the target star that can set upper limits on the amount of blended light each target may receive from nearby stars. In the process of characterizing the population of stars found near KOIs, we looked for a population of preferentially nearby neighbors that might represent physical binaries. However, we found no significant differences in separation from what we would expect given a randomly distributed population of background stars. As more targets are observed, we expect to obtain data on a larger sample of secondary stars, so will be better able to characterize their population.

The authors thank the *Kepler* Science Office at NASA/Ames for their continued support of the speckle observation program and their financial help with our EMCCD camera upgrade. We thank the anonymous referee for comments which led to an improved presentation. *Kepler* was selected as the 10th mission of the Discovery Program. Funding for this mission is provided by NASA.

REFERENCES

Batalha, N., et al. 2010, ApJ, 713, L103
Borucki, W. J., et al. 2010, Science, 327, 977
Borucki, W. J., et al. 2011, ApJ, in press, arXiv:1102.0541v2
Brown, T. M. 2003, ApJ, 593, L125
Brown, T. M., Latham, D. W., Everett, M. E., & Esquerdo, G. A. 2011, AJ, arXiv:1102.0342
Horch, E. P., Dinescu, D. I., Girard, T. M., van Altena, W. F., López, C. E., & Franz, O. G. 1996, AJ, 111, 1681
Horch, E. P., Falta, D., Anderson, L. M., DeSousa, M. D., Miniter, C. M., Ahmed, T., & van Altena, W. F. 2010, AJ, 139, 205
Horch, E. P., Gomez, S. C., Sherry, W. H., Howell, S. B., Ciardi, D. R., Anderson, L. M., & van Altena, W. F. 2011, AJ, 141, 45
Horch, E. P., Ninkov, Z., & Franz, O. G. 2001, AJ, 121, 1583
Horch, E. P., van Altena, W. F., Cyr, W. M., Kinsman-Smith, L., Srivastava, A., & Zhou, J. 2008, AJ, 136, 312
Horch, E. P., Veillette, D. R., Gallé, R. B., Shah, S. C., O'Reilly, G. V., & van Altena, W. F. 2009, AJ, 137, 5057
Tokovinin, A., & Cantarutti, R. 2008, PASP, 120, 170
Torres, G., et al. 2011, ApJ, 727, 24
Welsh, B. M. 1995, J. Opt. Soc. Am. A, 12, 1364